Prediction of the interfacial relationship between Y2O3 and TiN using first-principles calculations

Xiao Yun,[a] Xuejun Ren,*[b] Huixin Zheng,[a] Sha Liu,*[a] Yefei Zhou,[c] Jing Guo[d] and Qingxiang Yang *[a]

[a] State Key Laboratory of Metastable Materials Science & Technology, Hebei Key Lab for Optimizing Metal Product Technology and Performance, Yanshan University, Qinhuangdao, 066004, P. R. China. E-mail: Shaliu@ysu.edu.cn, qxyang@ysu.edu.cn; Fax: +86-335-807-4545; Tel: +86-335-838-7471

[b] School of Engineering, Liverpool John Moores University, Liverpool, L3 3AF, UK. E-mail: X.J.Ren@ljmu.ac.uk

[c] College of Mechanical Engineering, Yanshan University, Qinhuangdao, 066004, China

[d] Department of Mechanical Engineering, Glasgow Caledonian University, G4 0BA, UK

Abstract:

The hypereutectic Fe–Cr–C–N–Ti composite alloy has excellent wear resistance, in which TiN is an important strengthening phase. This paper aims to add the rare earth oxide Y2O3 to this alloy to refine TiN, and further enhance the service life of the alloy. The first-principles method was employed to investigate the interfacial relationship between Y2O3 and TiN. The mismatch degrees between the different low-index crystal planes of Y2O3 and TiN were calculated. Then, the plane with the minimum mismatch degree between Y2O3 and TiN was selected, and the surface convergence test was conducted. Based on this, an interfacial model of Y2O3//TiN was established, and its interfacial properties were calculated. The effectiveness of Y2O3 as the hetero-nucleation core of TiN was analyzed. The results show that the mismatch degree between the Y2O3 (111) plane and the TiN (110) plane is 8.19%, which indicates that the heteronucleation effect of Y2O3 on TiN is moderately effective. The surface model was constructed using the Y2O3(111) plane and the TiN(110) plane. It was found that when the layer number of the TiN(110) surface model reached 9, the surface energy converged to 2.75 J m_2. The interface adhesion work and interface energy of four Y2O3(111)//TiN(110) interfacial models were calculated. Among them, the interfacial adhesion energy of the O–N interface is the largest, which is 0.45 J m_2. Meanwhile, the interfacial energy of the O–N interface is the smallest, which is 3 J m_2. It indicates that the O–N interface model is the most stable. The chemical bonds in this model are mainly the combination of Ti–O ionic bonds and N–O covalent bonds. Therefore, Y2O3 meets the conditions to serve as the hetero-nucleation core of TiN and tends to form an O–N terminated hetero-nucleation interface, which can provide a theoretical basis for the development of a new hypereutectic Fe–Cr–C–N–Ti–Y2O3 alloy.

1. Introduction

In the hypereutectic Fe–Cr–C alloys, there are a large number of M7C3 type primary carbides,[1] which have high hardness[2] and excellent wear resistance,[3] and are the main strengthening phase in this alloy. Recently, the hypereutectic Fe–Cr–C alloys have attracted significant attention in the additive manufacturing field.[4,5] By using the hard-face-welding process, the hypereutectic Fe–Cr–C alloys are deposited on the surface of the workpieces, which can be used to fabricate workpieces of various shapes with high-wear-resistant surfaces.[6,7] However, during service, these large M7C3 type primary carbides tend to flake off from the surface of the workpieces, thereby reducing their service life.[8,9] With the rapid development of the additive manufacturing technology, especially its wide application in the surface remanufacturing field, the requirements for the service life of the hypereutectic Fe–Cr–C alloys have become increasingly higher. The preparation of the hypereutectic Fe–Cr–C alloy layers with stronger anti-spalling properties and higher wear resistance has become a bottleneck for the widespread application of this alloy.[10] In recent years, adding microalloying element Ti for improving the wear resistance of Fe–Cr–C–Ti alloy layers has been of growing interest. The research results show that the M7C3 type primary carbides can refine the hypereutectic Fe–Cr–C–Ti alloys by microalloying element Ti, so as to effectively improve their wear resistance.[11–14] Zhi et al.[12,13] investigated the influence of the element Ti on the microstructure and properties of the Fe–Cr–C–Ti alloy. They found that the TiC carbides precipitated earlier than theM7C3 type primary carbides and were capable of refining the M7C3 type primary carbides. Chung et al.[14] added the element Ti into Fe–25 wt%Cr–4 wt%C alloy. When the Ti addition was 2 wt%, the microstructure of the alloy could be refined, and it exhibited high wear resistance. These studies have shown that the microalloying element Ti not only refines the M7C3 type primary carbides, but also further enhances the wear resistance of the hypereutectic Fe–Cr–C–Ti alloys by forming TiC carbides in the alloy. However, the research also found that controlling the Ti content is of great significance. When the Ti content is too high, the Ti atoms can react with C atoms to form TiC carbides, which significantly reduces the C content in the matrix, and the volume fraction of M7C3 type primary carbides decreases markedly. In extreme cases, the hypereutectic Fe–Cr–C alloy may transform into the hypoeutectic Fe–Cr–C alloy, and the primary phase changes from M7C3 carbides to austenite, thereby severely reducing the wear resistance of the alloy.[15] As an interstitial atom, the N atom in iron-based alloys can interact with other alloying elements and improve the mechanical properties of the alloys.[16–18] Recently, Ding et al.[19] investigated the role of the alloying element N in the hypereutectic Fe–Cr–C alloy. They found that by jointly adding alloying elements Ti and N to the Fe–2.5C–25Cr alloy, the formation of Ti(C,N) carbide-nitrides could be promoted, ultimately leading to the refinement of M7C3 carbides. Therefore, we initially prepared a hypereutectic Fe–Cr–C–Ti–N alloy. It was found that in this alloy, while the C content in the matrix did not decrease, TiN nitrides could be generated, reducing the size of the M7C3 primary carbides from 30 μm to 10 μm. Compared with the Fe–Cr–C–Ti alloy without N, with the further increase of Ti content, the wear resistance of the alloy is further increased.[20]

Currently, the service environment of the hypereutectic Fe–Cr–C–Ti–N alloys is becoming increasingly demanding. As the external load and service time increase, the larger TiN nitrides on the surface of this alloy peel off, thereby reducing its service life.[21] The application of rare earth oxides in iron-based alloys has attracted considerable attention.[22,23] Guo et al.[24] investigated the effects of rare earth and Al on the microstructure and properties of Fe–Cr–C alloys, and found that the thick platelike carbides could be refined. Hou et al.[25] researched the influence of nano-sized rare earth particles on the microstructure and properties of Fe–Cr–C alloys, and confirmed that the M7C3 primary carbides transformed from thick plate-like to island-like or granular forms. Inspired by the above results, we added rare earth oxides to the hypereutectic Fe–Cr–C–Ti alloy and investigated their effects on M7C3 primary carbides and TiC carbides. It was found that as the addition of rare earth oxides increased, the M7C3 type primary carbides gradually became finer and the wear resistance was improved.[26] In particular, we also discovered that the rare earth oxide Y2O3 could further refine TiC, further refine the M7C3 type primary carbides, and thereby further enhance the wear resistance of the hypereutectic Fe–Cr–C–Ti alloy.[27,28] The above study leads us to consider whether rare earth oxide Y2O3 can be added to the hypereutectic Fe–Cr–C–N–Ti alloy to further refine the TiN nitride, thereby further improving the service life of the hypereutectic Fe–Cr–C–N–Ti alloy. However, it is difficult to observe the interfacial relationship between Y2O3 and TiN in the alloy by using experimental methods, and thus the mechanism by which Y2O3 refines TiN nitride cannot be revealed.

In recent years, the application of first-principles theory to the crystal interface relationships of materials has attracted much attention. Lv et al.[29] reported the electronic structure and formation energy of (Fe, M)3C (M = Cr/Mn/Co/Ni). Xiao et al.[30] conducted theoretical research on the stability and mechanical properties of Cr7C3 carbides. For this, we also employed first principles methods to study the crystal interface mismatch patterns between TiC and M7C3 carbides in the hypereutectic Fe–Cr–C–Ti alloy,[31,32] and explained the mechanism by which TiC carbides refine M7C3 carbides. Meanwhile, from our previous research work, the heterogeneous nucleation interface between Y2O3 and NbN was investigated via first principles method, and Y2O3 can serve as the hetero-nucleation core of NbN.[33] Therefore, the first-principles method is employed to explain the interface structure and interface bonding strength between Y2O3 and TiN at the atomic scale, and it is demonstrated that the mechanism by which Y2O3 refines TiN is feasible.

The first-principles method is employed in this paper to calculate the interface adhesion work, interfacial energy, electronic structure and bonding properties between Y2O3 and TiN carbides and analyzes the effectiveness of Y2O3 as the hetero-nucleation core of TiN. It provides a theoretical basis for the preparation of a new type of hypereutectic Fe–Cr–C–N–Ti–Y2O3 alloy.

2. Computational method

The Vienna ab initio simulation package (VASP) based on density functional theory[34] was used in this paper to optimize the bulk structures of TiN and Y2O3, and to calculate their surface and interface properties. The exchange–correlation energy was calculated and corrected using the generalized gradient approximation (GGA) functional improved by Perdew, Burke, Ernzerhorf (PBE) et al.[35] The interaction between the ion nucleus and valence electrons was described by the projector augmented waves (PAW).36 The appropriate plane wave truncation energy (Ecut) and Bragg zone K-point grid (Kmesh) were selected using convergence tests. The convergence test criteria were as follows: the energy change value was less than 1×10^{-5} eV $atom^{-1}$, the maximum force acting on each atom was lower than 0.02 eV A_1, and the maximum displacement was less than 1.0×10^{-3} A. Therefore, when optimizing the crystal structure of TiN, E_{cut} is set to 500 eV and K_{mesh} is set to 5x5x5. When optimizing the crystal structure of Y2O3, E_{cut} is set to 400 eV and K_{mesh} is set to 8 x8x8. When calculating the surface properties of Y2O3, E_{cut} is set to 400 eV and K_{mesh} is set to 8x8x1. Finally, when calculating their interface properties, E_{cut} is set to 500 eV and K_{mesh} is set to 5x5x1.

3. Results and analysis

3.1 Crystal structure and bulk properties of Y2O3 and TiN

The crystal structures of Y2O3 and TiN are shown in Fig. 1. Fig. 1(a) shows the crystal structure of Y2O3. Its structure belongs to the hexagonal crystal system and the space group is P63/mmc. The lattice constants are a = b = 3.68, c = 10.52 A, a = b =901, γ = 120°. Fig. 1(b) shows the crystal structure of TiN. Its structure belongs to the sodium chloride type and its space group is FM-3M. The lattice constants are a = b = c = 4.416 A, $\alpha=\beta=\gamma$ = 90°.

The bulk phase properties of Y2O3 are shown in Fig. 2. Fig. 2(a) shows the energy band structure of Y2O3. The position marked by the dotted line represents the Fermi level. The lowest point of the conduction band and the highest point of the valence band directly correspond to each other, and there is a band gap of approximately 5 eV between them, which indicates that Y2O3 has the properties of a direct band gap semiconductor. Fig. 2(b) shows the density of states of Y2O3. Due to the presence of peaks in the energy levels of Y atoms at the Fermi level, it is proved that there are a few metallic bonds. Within the range of _4 to 1 eV, the Y-d orbitals interact with the O-p orbitals, resulting in a resonance effect. Moreover, the peak intensity of the O-p orbitals is higher than that of the Y-d orbitals, which indicate that a Y-O ionic bond is formed between them. Within the range of 6 to 8 eV, the Y-d orbital interacts with the O-p orbital, and the peak intensity of the Y-d orbital is higher than that of the O-p orbital, which indicates the formation of Y-O ionic bonds between them. Therefore, the main types of chemical bonds in Y2O3 are metallic bonds and Y-O ionic bonds.

The bulk phase properties of TiN are shown in Fig. 3. Fig. 3(a) shows the energy band structure of TiN. The positions marked by the dotted lines correspond to the Fermi level. It can be observed that there is an overlapping area between the conduction band and the valence band of TiN, which indicates that there is no energy gap between them. The energy required for electron transition is very small, and it is easy for electrons to transition from the valence band to the conduction band, suggesting that TiN has certain metallic properties. Fig. 3(b) shows the density of states of TiN. It can be observed that there is a distinct peak at the Fermi level in the Ti-d orbitals, which proves the existence of metal bonds. Within the range of -8 to -2 eV, the N-p orbital and the Ti-d orbital undergo hybridization, and the peak intensity of the N-p orbital is higher than that of the Ti-d orbital, which indicates the formation of Ti-N ionic bonds. Within the range of -2 to 2.3 eV, there are peaks mainly in the Ti-d orbital, suggesting the formation of metallic bonds. Therefore, the main chemical bond types of TiN are metallic bonds and Ti–N ionic bonds.

3.2 Lattice mismatch degree between Y2O3 and TiN

According to Bramfitt 2D lattice mismatch theory,37 if the 2D lattice mismatch between the basal phase and the nucleating phase is less than 6%, the basal phase is able to play a very effective heterogeneous nucleation role with respect to the nucleating phase; with a mismatch degree of 6–12%, the basal phase plays a moderately effective heterogeneous nucleation role with respect to the nucleating phase and when the mismatch degree is larger than 12%, the basal phase cannot act as a heterogeneous nucleus for the nucleating phase. The two dimensional lattice mismatch is calculated as follows:37

$$\delta_{(hkl)_n}^{(hkl)_s} = \sum_{i=1}^{3} \left[\left(\left| d_{[uvw]_s}^{i} \cos\theta - d_{[uvw]_n}^{i} \right| \Big/ d_{[uvw]_n}^{i} \right) \Big/ 3 \right] \times 100\% \quad (1)$$

where (hkl)s is a low-index crystal plane in the nucleation substrate; [uvw]s is a low-index crystal direction in the low index crystal plane of the nucleation substrate; (hkl)n is a low index crystal plane in the nucleation phase; $[uvw]_n$ is a low index crystal direction in the low-index crystal plane of the nucleation phase; $d_{[uvw]n}$ is the distance of atoms in the crystal plane of $(hkl)_n$ along the direction of $[uvw]_n$; $d_{[uvw]s}$ is the atomic distance along the $[uvw]_s$ direction in the $(hkl)_s$ crystal plane.

Two groups of low-index crystal planes, namely Y2O3 and TiN, were selected to calculate their mismatch degrees. The results are listed in Table 1. The mismatch degree of the Y2O3(111) and TiN(110) planes is 8.19%, and that of the Y2O3(110) and TiN(111) planes is 8.22%, whose values range from 6% to 12%, which indicates that the role of Y2O3 as the hetero-nucleation core of TiN is moderately effective. Therefore, the Y2O3(111) plane and TiN(110) plane with a smaller mismatch degree (8.19%) are selected to construct the surface and interface model.

3.3 Interface properties of Y2O3 and TiN

3.3.1 Surface convergence test on Y2O3(111) and TiN(110). The surface models constructed for the Y2O3(111) and TiN(110) planes were conducted for the surface energy convergence tests. The four surface models constructed are shown in Fig. 4. There are three terminated surface models for the Y2O3(111) plane, namely Y-terminated, O1-terminated and O2-terminated surface models. Fig. 4(a)–(c) show three terminated surface models of the Y2O3 (111) plane. There is one terminated surface model for the TiN(110) plane. Fig. 4(d) depicts the surface model of TiN (110). The Y2O3(111) plane is a polar surface. The chemical potential calculation formula for the Y2O3 surface model is as follows:38

$$\mu_{\mathrm{Y_2O_3}}^{\mathrm{bulk}} = 2\mu_{\mathrm{Y}} + 3\mu_{\mathrm{O}} \qquad (2)$$

where $\mu_{\mathrm{Y_2O_3}}^{\mathrm{bulk}}$ represents the energy of the system after the structural relaxation of Y2O3 (111); μ_{Y} represents the chemical potential of the Y atom; μ_{O} represents the chemical potential of the O atom.

The surface energy sY2O3(111) formula for calculating the Y2O3 (111) surface is as follows:37

$$\sigma_{\mathrm{Y_2O_3(111)}} = \frac{1}{2A}(E_{\mathrm{slab}} - N_{\mathrm{Y}}\mu_{\mathrm{Y}} - N_{\mathrm{O}}\mu_{\mathrm{O}}) \qquad (3)$$

where E_{slab} represents the energy value (J) of the surface model with a certain number of atomic layers; A represents the surface area of the model (m2); NY represents the number of Y atoms in the Y2O3 (111) surface model; NO represent the number of oxygen atoms in the Y2O3 (111) surface model.

For the Y-terminated surface model, the calculation formula is as follows:

$$N_O = 2N_Y - 4 \tag{4}$$

For the O1-terminated surface model, the calculation formula is as follows:

$$N_O = 2N_Y \tag{5}$$

For the O2-terminated surface model, the calculation formula is as follows:

$$N_O = 2N_Y + 4 \tag{6}$$

By combining eqn (2)–(4), the final surface energy calculation formula for the Y-terminated surface model on the

Y2O3(111) plane is as follows:

$$\sigma_{Y_2O_3(111)} = \frac{1}{2A}\left[E_{slab} - \frac{1}{2}N_Y\mu_{Y_2O_3}^{bulk} - \left(\frac{1}{2}N_Y - 4\right)\mu_O\right] \tag{7}$$

By combining eqn (2), (3) and (5), the final surface energy calculation formula for the O1-terminated surface model on the Y2O3(111) plane is as follows:

$$\sigma_{Y_2O_3(111)} = \frac{1}{2A}\left[E_{slab} - \frac{1}{2}N_Y\mu_{Y_2O_3}^{bulk} - \frac{1}{2}N_Y\mu_O\right] \tag{8}$$

By combining eqn (2), (3) and (6), the final surface energy calculation formula for the O2 terminated surface model on the

Y2O3(111) plane is as follows:

$$\sigma_{Y_2O_3(111)} = \frac{1}{2A}\left[E_{slab} - \frac{1}{2}N_Y\mu_{Y_2O_3}^{bulk} - \left(\frac{1}{2}N_Y + 4\right)\mu_O\right] \tag{9}$$

The Y2O3(111) surface energy calculated results of the three terminated faces are listed in Tables 2–4. As the number of surface layers increases, the fluctuation range of the surface energy gradually becomes more stable. When the layer number of the Y-terminated surface model exceeds 13, its surface energy stabilizes and converges to 0.59 Jm_2.When the layer number of the O1-terminated surface model exceeds 9, its surface energy can stabilize and converge to 0.69 J m_2. The surface energy calculation result of the O2-terminated surface model is negative, which indicated that this model is unstable. Therefore, this model will not be considered in subsequent calculations. The TiN (110) plane is a non-polar surface. The surface energy sTiN(110) formula for calculating the TiN (110) surface is as follows:37

$$\sigma_{TiN(110)} = \frac{1}{2A}\left(E_{slab}^{N} - N\Delta E\right) \tag{10}$$

$$\Delta E = (E_{\mathrm{slab}}^{N} - E_{\mathrm{slab}}^{N-2})/2 \tag{11}$$

where E_{slab}^{N} represents the energy value (J) of the surface model with N atomic layers; E_{slab}^{N-2} represents the energy value (J) of the surface model with N-2 atomic layers; A represents the surface area of the model (m^2).

The calculated surface energy results are listed in Table 5. As the number of the surface layers increases, the fluctuation range of the surface energy gradually becomes more stable. When the layer number of the surface model reaches 9, the TiN (110) surface energy can be well converged to 2.75 J m^{-2}.

3.3.2 Interface model constructed of Y2O3(111) and TiN(110).

Four Y2O3(111)//TiN(110) interface models were constructed by selecting a 9-layer TiN (110) surface and respectively combining it with the Y-terminated surface of a 13-layer Y2O3 (111) and the O1-terminated surface of a 9-layer Y2O3 (111), as shown in Fig. 5. According to the different stacking methods, these four models were respectively named the Y–Ti, Y–N, O–Ti and O–N interface models.

The energy variation curves of the four interface models with the interface spacing after relaxation are shown in Fig. 6. It can be seen that the energy of the Y–Ti interface model is the lowest when the interface spacing is 2.6 A; the energy of the Y–N interface model is the lowest when the interface spacing is 2.8 A; the energy of the O–Ti interface model is the lowest when the interface spacing is 2.0 A; and the energy of the O–N interface model is the lowest when the interface spacing is 2.6 A.

3.3.3 Interface adhesive work and interface energy of Y2O3(111) and TiN(110).

The interface adhesive work (W_{ad}) is an important parameter for characterizing the strength of the interface bonding. For the interface model of Y2O3(111)//TiN(110), the calculation formula for Wad is as follows:39

$$W_{\mathrm{ad}} = \frac{1}{A}\left(E_{\mathrm{Y_2O_3}} + E_{\mathrm{TiN}} - E_{\mathrm{Y_2O_3/TiN}}\right) \tag{12}$$

where $E_{\mathrm{Y_2O_3/TiN}}$ E_{Y2O3}/TiN represents the energy value (J) of the Y2O3(111)//TiN(110) interface model; E_{Y2O3} represents the energy (J) of the Y2O3 (111) surface model; E_{TiN} (J) represents the energy (J) of the TiN (110) surface model; and A represents the interface area (m2).

The interface energy (g) corresponds to the difficulty of heterogeneous nucleation at the interface. The calculation formula for g of the four interface models is as follows:40

$$\gamma = \sigma_{\mathrm{Y_2O_3}} + \sigma_{\mathrm{TiN}} - W_{\mathrm{ad}} \tag{13}$$

where sY2O3 represents the surface energy (J m^{-2}) of the Y2O3 (111) surface model; σ_{TiN} represents the surface energy (J m^{-2}) of the TiN (110) surface model. The W_{ad} and g values of the four Y2O3(111)//TiN(110) interface models are shown in Fig. 7. The W_{ad} sequence of the four interface models is as follows: $W_{adO\text{–}N} > W_{adO\text{–}Ti} > W_{adY\text{–}N} > W_{adY\text{–}Ti}$.

The γ sequence of the four interface models is as follows: $\gamma_{O\text{–}N} < \gamma_{O\text{–}Ti} < \gamma_{Y\text{–}N} < \gamma_{Y\text{–}Ti}$.

It can be seen that both the O-terminated surface of Y2O3(111) and the interface model on the TiN(110) surface are relatively stable. Among them, the W_{ad} value of the O–N interface is the largest, which is 0.45 J m_2. Meanwhile, the g value of the O–N interface is the smallest, which is 3 J m_2. Therefore, the O–N interface is the most stable.

3.3.4 Interface model bonding characteristics of Y2O3(111) and TiN(110).

By calculating the charge density, differential charge density and partial densities of states (PDOS) of the Y2O3(111)//TiN(110) interface model, the bonding characteristics of the Y2O3(111)//TiN(110) interface model are analyzed, and the stability of the interface is further determined. The charge densities of the (100) section of Y2O3(111)//TiN(110) interface models are shown in Fig. 8. In Fig. 8, the charge accumulation areas are indicated by the red regions, and the charge depletion areas are indicated by the blue regions. The color changes from blue to red to represent the increasing charge density. Fig. 8(a) shows the charge density of the O–Ti interface in Y2O3(111)//TiN(110) interface model. It can be seen that at the interface, Ti atoms relax downward while O atoms relax upward. The charge density around the O atoms is high, while that around the Ti atoms is low. A chemical bond is formed between them. Fig. 8(b) shows the charge density of the O–N interface in the Y2O3(111)//TiN(110) interface model. It can be seen that at the interface, the diffusion phenomenon of O atoms and Ti atoms at the interface is more obvious, indicating that the chemical bond formed between the two is stronger.

The formula for calculating the differential charge density is as follows:

$$\rho_{d} = \rho_{tot} - \rho_{Y_2O_3} - \rho_{TiN} \qquad (14)$$

where rtot represents the total charge density in the interface model; rY2O3 represents the charge density of the individual Y2O3(111) plane within the same interface model; rTiN represents the charge density of the individual TiN(110) plane within the same interface model.

The differential charge densities of the (100) section of Y2O3(111)//TiN(110) interface models are shown in Fig. 9. In Fig. 9, the charge accumulation areas are indicated by the red regions, and the charge depletion areas by the blue regions. The color ranges from blue to red to represent the increasing charge density. Fig. 9(a) shows the differential charge density at the O–Ti interface. It can be observed that there is a depletion zone of charge around the Ti atoms at the interface, with a lower charge density. There are also numerous charge accumulation zones around the O atoms, with a higher charge density. This indicates that ionic bonds have formed between them. Fig. 9(b) shows the differential charge density at the O–N interface. It can be seen that compared with Fig. 9(a), the atomic relaxation phenomenon at the interface is more obvious, and the formed charge accumulation area and charge depletion area are also larger. This indicates that the ionic bond strength formed at the O–N interface is higher than that of the O–Ti interface model, and the interface combination is more stable.

The partial densities of states (PDOS) diagrams of Y2O3(111)//TiN(110) interface models are shown in Fig. 10. Both interfaces have significant peaks in the Fermi level Ti-d orbitals, which indicate that both interfaces possess metallic properties. Fig. 10(a) shows the PDOS of the O–Ti interface. With in the range of _5.7 to _4 eV, there are peaks at the O-p orbitals and Ti-d orbitals, and the peak intensity of the O-p orbitals is higher

than that of the Ti-d orbitals, which indicate the formation of Ti–O ionic bonds between them. Within the range of -4 to -2 eV, peaks appear at the N-p orbitals and O-p orbitals, and the intensities of the two orbitals are approximately the same, suggesting the formation of N–O covalent bonds between them. Fig. 10(b) shows the PDOS of the O–N interface. Within the range of _5 to _3 eV, there are peaks at the O-p orbital and the

Ti-d orbital, and the peak intensity of the O-p orbital is higher than that of the Ti-d orbital, which indicate the formation of Ti–O ionic bonds between them. Within the range of -3.7 to 2 eV, peaks appear at the N-p orbital and the O-p orbital, and the peak intensities of the two orbitals are approximately the same, indicating the formation of N–O covalent bonds between them. Within the range of -2 to 0.2 eV, there are peaks at the O-p orbital and the Ti-d orbital, and the peak intensity of the O-p orbital is higher than that of the Ti-d orbital, which indicate the formation of Ti–O ionic bonds between them.

4. Conclusions

(1) The minimum mismatch degree between the Y2O3 (111) plane and TiN (110) plane is 8.19%, which indicates that the heterogeneous nucleation effect of Y2O3 on TiN is moderatelyeffect ive.

(2) The surface models of Y2O3 (111) and TiN (110) were selected to conduct surface energy convergence tests. It was found that when the number of layers of the TiN (110) surface model reached 9, the surface energy converged to 2.75 J m_2.

(3) The interfacial adhesion work and interfacial energy of four Y2O3(111)//TiN(110) interface models were calculated. Among them, the interfacial adhesion work of the O–N interface is the largest, which is 0.45 J m^{-2}. Meanwhile, the interfacial energy of the O–N interface is the smallest, which is 3 J m^{-2}. Therefore, the O–N interface model is the most stable. Its chemical bonds are mainly the combination of Ti–O ionic bonds and N–O covalent bonds.

Author contributions

Xiao Yun: conceptualization, methodology, investigation, writing – original draft. Xuejun Ren: resources, project administration, funding acquisition. Huixin Zheng: data curation, visualization. Sha Liu: methodology, resources. Yefei Zhou: methodology, resources. Jing Guo: methodology. Qingxiang Yang: conceptualization, investigation, methodology, resources, software, funding acquisition, writing – review & editing, supervision.

Conflicts of interest

The authors declare that they have no known competing financial interests or personal relationships that could have appeared to influence the work reported in this paper.

Data availability Data will be made available on request.

Acknowledgements

The authors would like to express their gratitude for projects supported by the National Natural Science Foundation of China (No. 52371077), the Hebei Natural Science Foundation (E2025203128), and the European Union's Research and Innovation Program Horizon Europe under the Marie Skłodowska-Curie Actions grant agreement (No. 101129996, SynAM) and UKRI Engineering and Physical Sciences Research Council.

References

1 C. M. Chang, C. C. Lin and C. C. Hsieh, Micro-structural characteristics of Fe-40 wt% Cr-xC hardfacing alloys with [1.0-4.0 wt%] carbon content, J. Alloys Compd., 2009, 487, 83–89.

2 X. Wu, J. Xing, H. Fu and X. Zhi, Effect of titanium on the morphology of primary M7C3 carbides in hypereutectic high chromium white iron, Mater. Sci. Eng., A, 2007, 457, 180–185.

3 J. Janovec, V. Magula, A. Holy´ and A. Vy´rostkova´, Influence of long-term isothermal exposures upon M7C3 carbide changes in 2.7Cr0.6Mo0.3V steel, Scr. Med., 1992, 26, 1303–1308.

4 P.Ku¨rnsteiner, P. B. Vila and P. Bajaj, Designing an Fe-Ni-Ti maraging steel tailor-made for laser additive manufacturing, Addit. Manuf., 2023, 73, 103647.

5 C. Ladd, J. H. So, J. Muth and M. D. Dickey, 3D printing of free standing liquid metal microstructures, Adv. Mater., 2013, 25, 5081–5087.

6 A. Zikin, I. Hussainova and C. Katsich, Advanced chromium carbide-based hardfacings, Surf. Coat. Technol., 2012, 206, 4270–4278.

7 D. S. Liu, R. P. Liu and Y. H. Wei, Comparative behaviour of cobalt and iron base hardfacing Alloys, Surf. Eng., 2012, 28, 338–344.

8 B. S. Yilbas, S. S. Akhtar and C. Karatas, Laser gas assisted melting of preprepared alumina surface including Tic particles at surface, Surf. Eng., 2011, 27, 470–476.

9 X. W. Qi, Z. N. Jia and Q. X. Yang, Effects of vanadium additive on structure property and tribological performance of high chromium cast iron hardfacing metal, Surf. Coat. Technol., 2011, 205, 5510–5514.

10 A. Wiengmoon, T. Chairuangsri, A. Brown, R. Brydson, D. V. Edmonds and J. T. H. Pearce, Microstructural and crystallographical study of carbides in 30 wt% Cr cast irons, Acta Mater., 2005, 53, 4143–4154.

11 X. Zhi, J. Xing and H. Fu, Effect of niobium on the as-cast microstructure of hypereutectic high chromium cast iron, Mater. Lett., 2008, 62, 857–860.

12 X. Zhi, J. Xing and Y. Gao, Effect of heat treatment on microstructure and mechanical properties of a Ti-bearing hypereutectic high chromium white cast iron, Mater. Sci.Eng., A, 2008, 487, 171–179.

13 X. Zhi, J. Xing and H. Fu, Effect of titanium on the as-cast microstructure of hypereutectic high chromium cast iron, Mater. Charact., 2008, 59, 1221–1226.

14 R. J. Chung, X. Tang and D. Y. Li, Effects of titaniumaddition on microstructure and wear resistance of hypereutectic high chromium cast iron Fe–25 wt% Cr–4 wt% C, Wear, 2009, 267, 356–361.

15 Y. F. Zhou, Y. L. Yang, J. Yang, F. F. Hao, D. Li, X. J. Ren and Q. X. Yang, Effect of Ti additive on (Cr, Fe)7C3 carbide in arc surfacing layer and its refined mechanism, Appl. Surf. Sci., 2012, 258, 6653–6659.

16 V. V. Kanta, A. F. Delaunois and F. Delaunois, Application of nitriding to electroless nickel-boron coatings: Chemical and structural effects; mechanical characterization; corrosion resistance, Mater. Des., 2012, 39, 269–278.

17 G. Saller, H. K. Spiradek, C. Scheu and H. Clemens, Microstructural evolution of Cr-Mn-N austenitic steels during cold work hardening, Mater. Sci. Eng., A, 2006, 427, 246–254.

18 C. X. Li and T. Bell, Corrosion properties of active screen plasma nitrided 316 austenitic stainless steel, Corros. Sci., 2004, 46, 1527–1547.

19 H. S. Ding, S. Q. Liu, H. L. Zhang and J. J. Guo, Improving impact toughness of a high chromium cast iron regarding joint additive of nitrogen and titanium, Mater. Des., 2016, 90, 958–968.

20 J. B. Wang, T. T. Liu, Y. F. Zhou, X. L. Xing, S. Liu, Y. L. Yang and Q. X. Yang, Effect of nitrogen alloying on the microstructure and abrasive impact wear resistance of Fe-Cr-C-Ti-Nb hardfacing alloy, Surf. Coat. Technol., 2017, 309, 1072–1080.

21 J. B. Wang, X. L. Xing, Y. F. Zhou, S. C. Liu, X. W. Qi and Q. X. Yang, Formation mechanism of ultrafine M7C3 carbide in a hypereutectic Fe-25Cr-4C-0.5Ti-0.5Nb-0.2N-2LaAlO3 hardfacing alloy layer, J. Mater. Res. Technol.,2020, 9(4), 7711–7720.

22 Y. W. Kim, Y. S. Chun, T. Nishimura, M. Mitomob and Y. H. Lee, High-temperature strength of silicon carbide ceramics sintered with rare-earth oxide and aluminum nitride, Acta Mater., 2007, 55, 727–736.

23 T. Mori, D. R. Ou, J. Zou and J. Drennan, Present status and future prospect of design of Pt–cerium oxide electrodes for fuel cell applications, Prog. Nat. Sci., 2012, 22, 561–571.

24 E. J. Guo, L. P. Wang, Y. C. Huang and Y. K. Fu, Effects of rare earths and A1 on structure and performance of high chromium cast iron containing wolfram, J. Rare Earths, 2006, 24, 238–242.

25 Y. C. Hou, Y. Wang, Z. Y. Pan and L. L. Yu, Influence of rare earth nanoparticles and inoculants on performance and microstructure of high chromium cast iron, J. Rare Earths, 2012, 30, 283–288.

26 Y. F. Zhou, Y. L. Yang, Y. W. Jiang, J. Yang, X. J. Ren and Q. X. Yang, Fe-24 wt%Cr-4.1 wt%C hardfacing alloy: microstructure and carbide refinement mechanisms with ceria additive, Mater. Charact., 2012, 72, 77–86.

27 Z. J. Shi, S. Liu, Y. K. Gao, Y. F. Zhou, X. L. Xing, X. J. Ren and Q. X. Yang, Mechanism of Y2O3 as heterogeneous nucleus of TiC in hypereutectic Fe-CrC-Ti-Y2O3 coating: First principle calculation and experiment research, Mater. Today Commun., 2017, 13, 80–91.

28 Z. J. Shi, W. Shao, T. S. Hu, C. C. Zhao, X. L. Xing, Y. F. Zhou and Q. X. Yang, Adhesive sliding and interfacial property of YAlO3/TiC interface: A first principles investigation, J. Alloys Compd., 2019, 805, 1052–1059.

29 Z. Q. Lv, F. C. Zhang and S. H. Sun, First-principles study on the mechanical, electronic and magnetic properties of Fe3C. Comp, Mater. Sci., 2008, 44, 690–694.

30 B. Xiao, J. D. Xing and J. Feng, A comparative study of Cr7C3, Fe3C and Fe2B in cast iron both from ab initio calculations and experiments, J. Phys. D: Appl. Phys., 2009, 42, 115415.

31 C. C. Zhao, X. L. Xing, J. Guo, Z. J. Shi, Y. F. Zhou, X. J. Ren and Q. X. Yang, Microstructure and wear resistance of (Nb,Ti)C carbide reinforced Fe matrix coating with different Ti contents and interfacial properties of (Nb,Ti)C/a-Fe, Appl. Surf. Sci., 2019, 494, 600–609.

32 S. Liu, Y. F. Zhou, X. L. Xing, J. B. Wang and Q. X. Yang, Refining effect of TiC on primary M7C3 in hypereutectic FeeCreC harden-surface welding coating: Experimental research and first principles calculation, J. Alloys Compd., 2017, 691, 239–249.

33 H. X. Zheng, C. M. Zhao, Q. Z. He, Y. N. He, X. J. Ren, J. Guo and Q. X. Yang, Insights into heterogeneous nucleation interface of Y2O3//NbN via first principles calculation, Mater. Today Commun., 2024, 39, 108583.

34 G. Kresse and J. Hafner, Ab initio molecular dynamics for liquid metals, Phys. Rev. B: Condens. Matter Mater. Phys., 1993, 47, 558–561.

35 J. P. Perdew, K. Burke and M. Ernzerhof, Generalized gradient approximation made simple, Phys. Rev. Lett., 1997, 78, 1396.

36 D. Joubert, From ultrasoft pseudopotentials to the projector augmented-wave method, Phys. Rev. B: Condens. Matter Mater. Phys., 1999, 59, 1758–1775.

37 B. L. Bramfitt, The effect of carbide and nitride additions on the heterogeneous nucleation behavior of liquid iron, Metall. Trans., 1970, 1, 1987–1995.

38 Z. J. Shi, S. Liu, J. Guo and Q. X. Yang, Investigation on heterogeneous nucleation substrate of Y2O3 as NbC in hypereutectic Fe–Cr–C hard facing coating by experiment and firstprinciples calculation, J. Mater. Sci., 2019, 54, 10102–10118.

39 F. Chen, H. Jiang and Y. Zhang, First-principles calculation of bonding and hydrogen trapping mechanism of Fe3C/a-Fe interface, J. Mater. Res. Technol., 2023, 26, 6782–6793.

40 J. Wang, J. Yang and C. Wang, First-principles calculation on LaAlO3 as the heterogeneous nucleus of TiC, Comp, Mater. Sci., 2015, 101, 108–114.

Table 1 Mismatch degree of the low-index planes of Y_2O_3 and TiN

Matching plane	$Y_2O_3(111)//TiN(110)$			$Y_2O_3(110)//TiN(111)$		
$[uvw]_{Y_2O_3}$	$[1\bar{1}0]$	$[1\bar{1}2]$	$[1\bar{1}1]$	$[1\bar{1}2]$	$[\bar{1}11]$	$[\bar{1}14]$
$[uvw]_{TiN}$	$[001]$	$[1\bar{1}0]$	$[1\bar{1}1]$	$[1\bar{1}0]$	$[1\bar{1}2]$	$[10\bar{1}]$
θ (°)	0	0	0	0	0	5.264
$d_{Y_2O_3}$ (Å)	3.84	6.652	7.681	6.652	9.407	11.522
d_{TiN} (Å)	4.238	5.993	7.34	5.993	10.86	11.986
δ (%)	8.19			8.22		

Table 2 Surface energy of the Y-terminated surface model on the Y_2O_3 (111) plane (J m^{-2})

Layer	4	7	10	13	16
$Y_2O_3(111)$	3.76	1.27	0.54	0.59	0.58

Table 3 Surface energy of the O1-terminated surface model on the Y_2O_3 (111) plane (J m^{-2})

Layer	3	6	9	12	15
$Y_2O_3(111)$	0.81	0.69	0.69	0.68	0.67

Table 4 Surface energy of the O2-terminated surface model on the Y_2O_3 (111) plane (J m^{-2})

Layer	5	8	11	14	17
$Y_2O_3(111)$	−0.81	−1.18	−1.32	−1.19	−1.12

Table 5 Surface energy of the TiN(110) surface model (J m^{-2})

Layer	5	7	9	11	13
TiN(110)	2.82	3.09	2.75	2.76	2.81

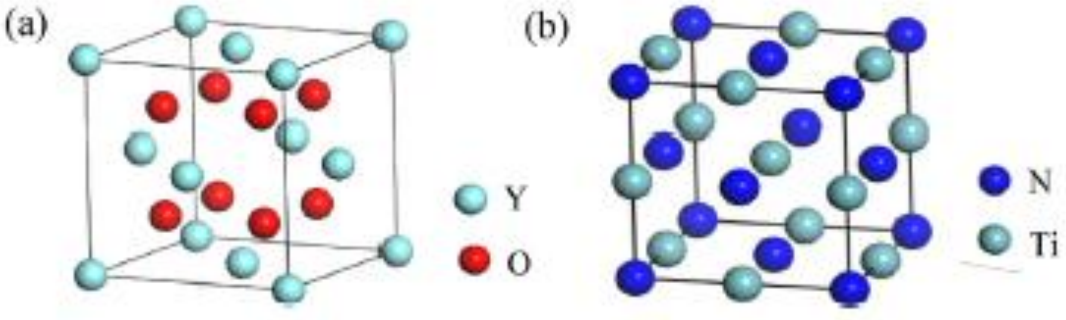

Fig. 1 Crystal structures of Y2O3 and TiN: (a) Y2O3; (b) TiN.

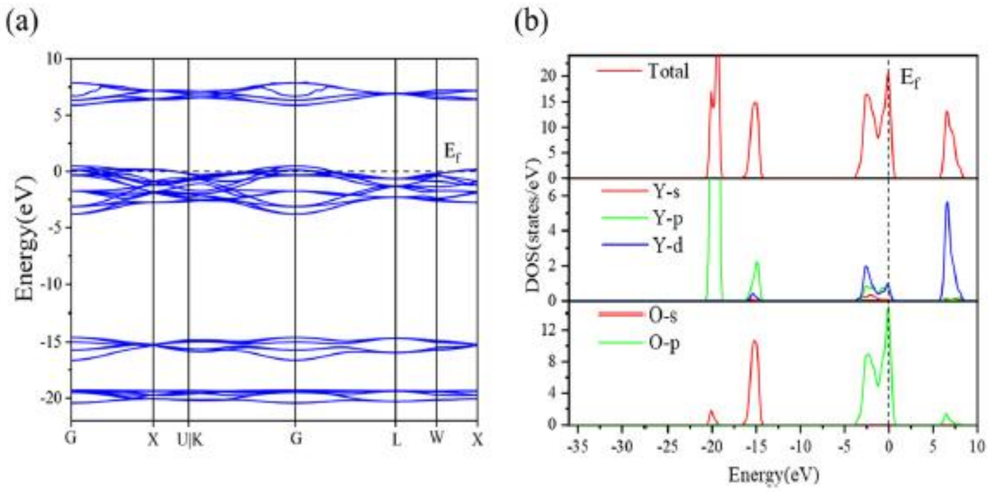

Fig. 2 Bulk phase properties of Y2O3: (a) energy band structure; (b) density of states diagram.

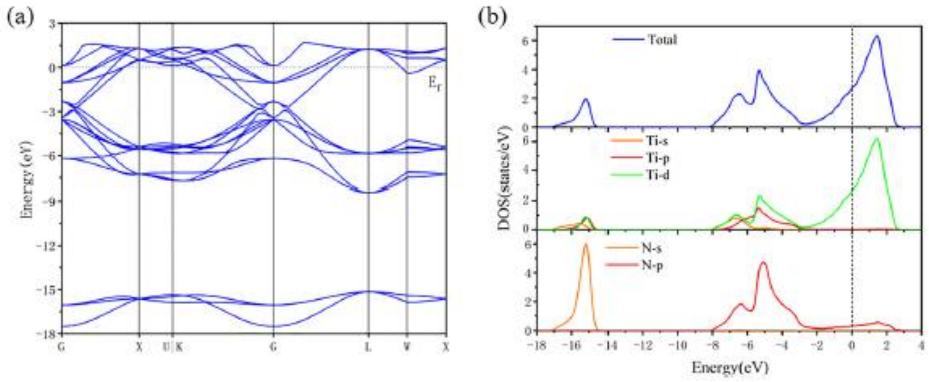

Fig. 3 Bulk phase properties of TiN: (a) energy band structure; (b) density of states diagram.

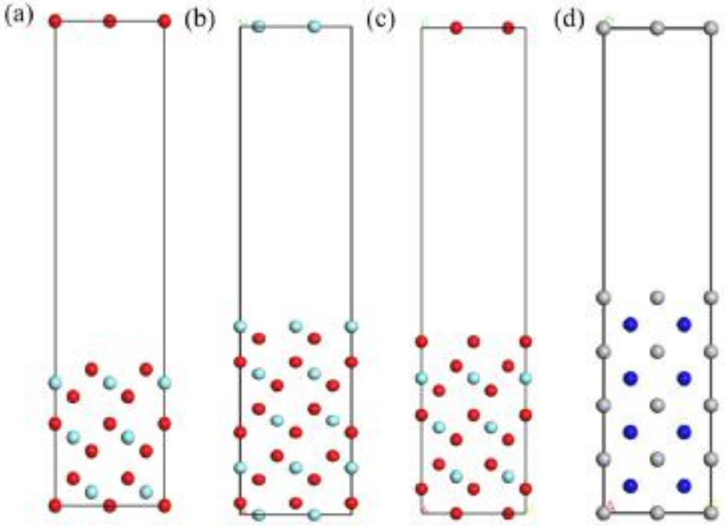

Fig. 4 Surface models of Y2O3 and TiN: (a) Y2O3(111) with Y atom termination; (b) Y2O3(111) with O1 atom termination; (c) Y2O3(111) with O2 atom termination; (d) TiN(110).

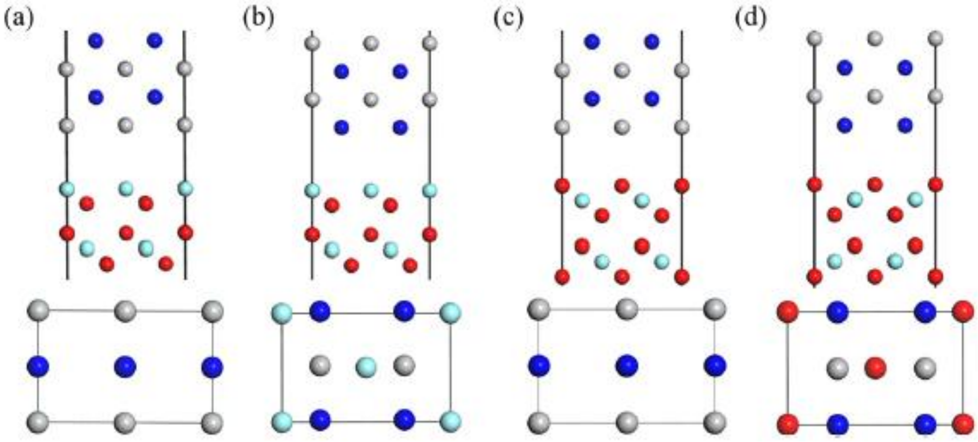

Fig. 5 Four interface models of Y2O3 and TiN interface. (a) Y–Ti; (b) Y–N; (c) O–Ti; (d) O–N.

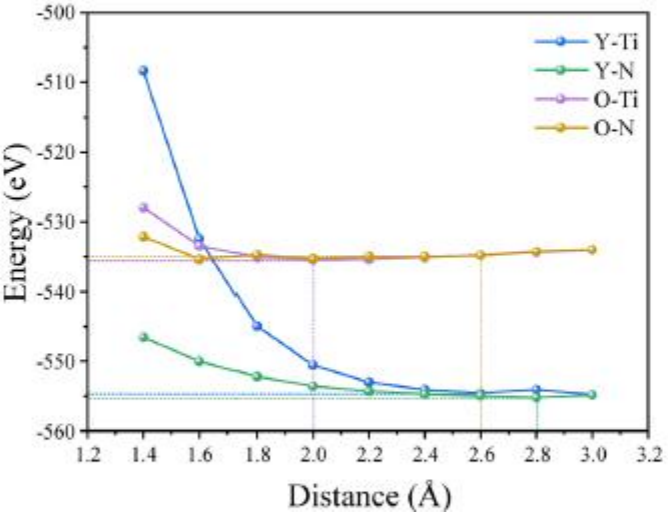

Fig. 6 Energy variation diagrams of four Y2O3 (111) and TiN (110) interface models with respect to the interface spacing.

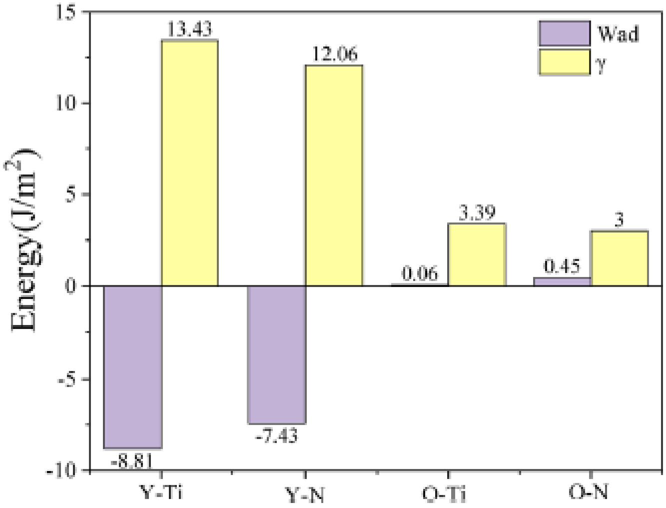

Fig. 7 Wad and g of four Y2O3 (111) and TiN (110) interface models.

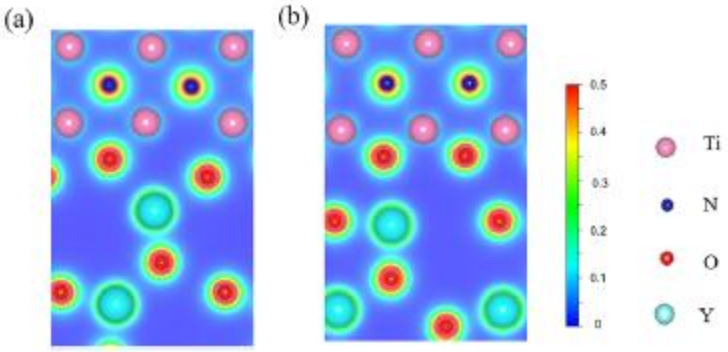

Fig. 8 Charge density map of the (100) section of Y2O3 (111) and TiN (110) interface models: (a) O–Ti interface; (b) O–N interface.

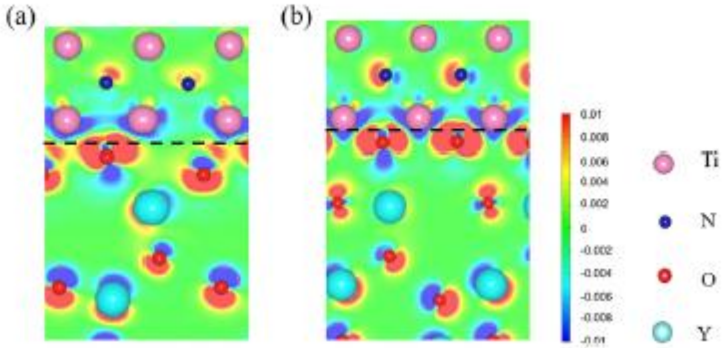

Fig. 9 Differential charge density of the (100) section of Y2O3 (111) and TiN (110) interface models: (a) O–Ti interface; (b) O–N interface.

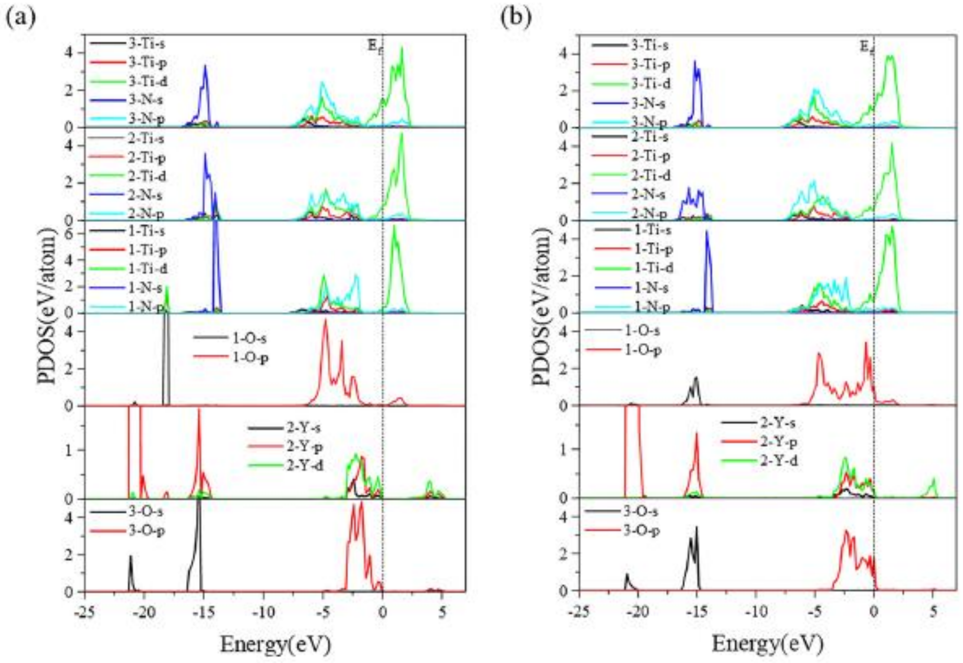

Fig. 10 PDOS of Y_2O_3 (111) and TiN (110) interface models: (a) O–Ti interface; (b) O–N interface.